

Generation of a large orbital angular momentum beam via an optical fiber winding around a curved path and its application

Wei-Han Tan(谭维翰), Chao-Ying Zhao(赵超樱), Yi-Chao Meng(孟义朝), and Qi-Zhi Guo(郭奇志)
Citation: Chin. Phys. B, 2021, 30 (**10**): 104208. DOI: 10.1088/1674-1056/abefc9
Journal homepage: http://cpb.iphy.ac.cn; http://iopscience.iop.org/cpb

What follows is a list of articles you may be interested in

Visible-light all-fiber vortex lasers based on mode selective couplers

Chuchu Dong(董楚楚), Jinhai Zou(邹金海), Hongjian Wang(王鸿健), Han Yao(尧涵), Xianglong Zeng(曾祥龙), Yikun Bu(卜轶坤), Zhengqian Luo(罗正钱)
Chin. Phys. B, 2020, 29 (**9**): 094204. DOI: 10.1088/1674-1056/aba278

Hollow and filled fiber bragg gratings in nano-bore optical fibers

Yong-Xin Zhang(张永欣), Sheng Liang(梁生), Qian-Qing Yu(余倩卿), Zheng-Gang Lian(廉正刚), Zi-Nian Dong(董梓年), Xuan Wang(王旋), Yu-Qin Lin(林裕勤), Yu-Qi Zou(邹郁祁), Kun Xing(邢坤), Liu-Yan Liang(梁柳雁), Xiao-Ting Zhao(赵小艇), Li-Jing Tu(涂立静)
Chin. Phys. B, 2019, 28 (**7**): 074210. DOI: 10.1088/1674-1056/28/7/074210

Extraordinary transmission and reflection in *PT*-symmetric two-segment-connected triangular optical waveguide networks with perfect and broken integer waveguide length ratios

Jia-Ye Wu(吴嘉野), Xu-Hang Wu(吴栩航), Xiang-Bo Yang(杨湘波), Hai-Ying Li(李海盈)
Chin. Phys. B, 2019, 28 (**10**): 104208. DOI: 10.1088/1674-1056/ab3f92

Observation of 550 MHz passively harmonic mode-locked pulses at L-band in an Er-doped fiber laser using carbon nanotubes film

Qianqian Huang(黄千千), Chuanhang Zou(邹传杭), Tianxing Wang(王天行), Mohammed Al Araimi, Aleksey Rozhin, Chengbo Mou(牟成博)
Chin. Phys. B, 2018, 27 (**9**): 094210. DOI: 10.1088/1674-1056/27/9/094210

Gamma-radiation effects in pure-silica-core photonic crystal fiber

Wei Cai(蔡伟), Ningfang Song(宋凝芳), Jing Jin(金靖), Jingming Song(宋镜明), Wei Li(李伟), Wenyong Luo(罗文勇), Xiaobin Xu(徐小斌)
Chin. Phys. B, 2017, 26 (**11**): 114211. DOI: 10.1088/1674-1056/26/11/114211

Generation of a large orbital angular momentum beam via an optical fiber winding around a curved path and its application*

Wei-Han Tan(谭维翰)[1], Chao-Ying Zhao(赵超樱)[2,3,†], Yi-Chao Meng(孟义朝)[4], and Qi-Zhi Guo(郭奇志)[1]

[1] *Department of Physics, Shanghai University, Shanghai* 200444, *China*
[2] *College of Science, Hangzhou Dianzi University, Hangzhou* 310018, *China*
[3] *State Key Laboratory of Quantum Optics and Quantum Optics Devices, Institute of Opto-Electronics, Shanxi University, Taiyuan* 030006, *China*
[4] *Institute of Fiber Optics, Shanghai University, Shanghai* 200444, *China*

(Received 7 January 2021; revised manuscript received 11 March 2021; accepted manuscript online 18 March 2021)

Many papers have been published on the study of orbital angular momentum (OAM) of the laser modes based on the Laguerre–Gaussian (LG) beam and helical phase plate or rotating cylindrical lens, and the principal ray of the LG beam remains straight line. These ways are difficult to get a large OAM modes. In this paper, we propose a novel method to prepare a large OAM modes when the light propagates through a optical fiber winding around a curved path, and establish a theoretical framework based on the principal ray path changing. Firstly, we investigate three kinds of winding structure. Secondly, based on the analytical solutions and numerical calculations, we can find that the spiral body can achieve a large OAM temporal pulse. At the same time, based on the zero OAM diffraction diagram, we can obtain an improvement of resolving power beyond Rayleigh's criterion. Finally, applying a large OAM diffraction pattern to realize 12-bitencodes, we can obtain a high-security optical information transfer system.

Keywords: fiber optics, orbital angular momentum (OAM), differential Fernet equation, Rayleigh criterion

PACS: 42.81.Qb, 42.50.Tx, 02.40.−k **DOI:** 10.1088/1674-1056/abefc9

1. Introduction

The generation of the optical beams with orbital angular momentum (OAM) have attracted much attention in optics communication and quantum key distribution. In these applications, we find that the OAM mode can be detected by the discrete "twisting" rate of helical phase. Up to now, the traditional methods of preparing OAM beam include rotating cylindrical lens, helical phase plates, and fiber[1–5] when the wave-front phase is changing and the principal ray is basically unchanged,[6–8] and it is difficult to obtain a large OAM modes. In order to solve the problem, we establish a theoretical framework on the condition that the principal ray is changing and the wave-front phase is basically unchanged.[9,10] The light emitted from the cylindrical spiral wave-guide can carry a high-order OAM modes.[11] In this paper, we achieve a large OAM modes in an optical fiber winding around a curved path of spiral body. We calculate the large OAM modes in the flowing coordinate system (α,β,γ). Applying the large OAM diffraction patterns, we can obtain a 12-bitencodes, and finally provide a high security information transfer system. At the same time, according to analyzing the zero OAM diffraction patterns, we find that our method can improve the spatial resolving power beyond the Rayleigh limiting.

The organization is as follows: The notation and parameters of the coordinate system, and types of winding around a curved path are presented in Section 2; subsequently, analytical solution is calculated in Section 3; numerical calculation of the OAM via an optical fiber winding around a curved path is given in Section 4; the diffraction patterns calculation and applications are given in Section 5; an experimental scheme for observation of a large OAM beam is proposed in Section 6; finally, the conclusion and discussion are given in Section 7.

2. The winding-types around the spiral body and the coordinate systems

The fiber winding around the circular cylinder body results in a spiral form,[9] but it does not mean that the circular cylinder body itself be a spiral form. The circular cones are depicted in Figs. 1(a)–1(c); and Figs. 1(d)–1(f) are the spiral curves of optical fiber around the circular cones.

In the static coordinate system, the curves as a function of θ can be expressed by

$$\boldsymbol{r} = (a(\theta)\cos[f(\theta)], a(\theta)\sin[f(\theta)], b\theta), \tag{1}$$

where $a(\theta)$ and $b\theta$ denote the radius and the axis of the circular cone function, respectively, and $f(\theta)$ is the winding function. As shown in Figs. 1(d)–1(f), we call the types of spiral curves, "Exponential", "Gaussian", and "Flower", respectively:

$$\text{Exponential}: \quad a_{\mathrm{E}}(\theta) = a_0\theta\,\mathrm{e}^{-l_1|\theta|}, \quad f(\theta) = \frac{\theta}{1+l_2\theta},$$

*Project supported by the National Natural Science Foundation of China (Grant No. 11504074) and the State Key Laboratory of Quantum Optics and Quantum Optics Devices, Shanxi University (Grant No. KF202004).

†Corresponding author. E-mail: zchy49@163.com

© 2021 Chinese Physical Society and IOP Publishing Ltd

$$
\begin{aligned}
&r_z = b\theta, \quad 0 < \theta < \infty;\\
\text{Gaussian}: \quad &a_{\mathrm{G}}(\theta) = a_0 \mathrm{e}^{-l_1\theta^2}, \quad f(\theta) = \frac{\theta}{1+l_2\theta},\\
&r_z = b\theta, \quad -\infty < \theta < \infty;\\
\text{Flower}: \quad &a_{\mathrm{F}}(\theta) = a_0 \cos[n\theta], \quad f(\theta) = \frac{\theta}{1+l_2\theta},\\
&r_z = b\theta, \quad n = \text{integer}, \quad -\infty < \theta < \infty,
\end{aligned} \tag{2}
$$

where the constants a_0, $l_1 > 0$, and n control the characteristic of circular cone; $l_2 \geq 0$ controls the winding-type. $l_2 = 0$, $l_2 > 0$, and $l_2 = \infty$ denote the homogeneous winding, inhomogeneous winding, and stop-winding, respectively.

As shown in Figs. 2(a) and 2(b), we adopt two coordinate systems in order to perform the following calculation, the first is static coordinate system $\boldsymbol{r} = r_x\boldsymbol{x} + r_y\boldsymbol{y} + r_z\boldsymbol{z}$, where the fixed unit vectors $(\boldsymbol{x}, \boldsymbol{y}, \boldsymbol{z})$ are perpendicular to each other, and the second is flowing coordinate system $\boldsymbol{r} = \xi\boldsymbol{\beta} + \eta\boldsymbol{\gamma} + \zeta\boldsymbol{\alpha}$, where the moving unit vectors $(\boldsymbol{\beta}, \boldsymbol{\gamma}, \boldsymbol{\alpha})$ are perpendicular to each other, which along a spiral curve of optical fiber as shown in Figs. 1(d)–1(f).

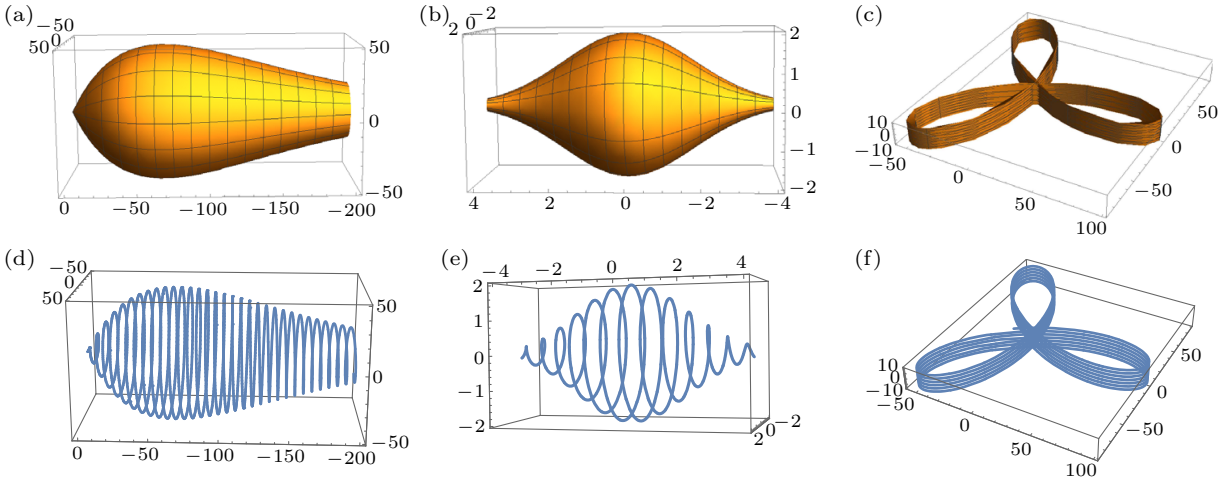


Fig. 1. Circular cones (a)–(c), and the spiral curves of optical fiber around the circular cones (d)–(f).

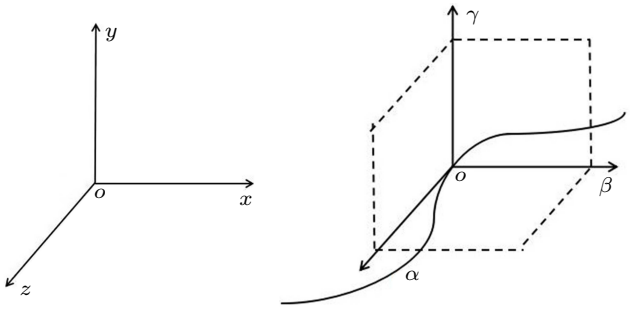


Fig. 2. Static coordinate system (a) and flowing coordinate system (b).

3. Analytical solutions for the OAM

In generally, the curved path can be written by the static coordinate system $\boldsymbol{r} = r_x\boldsymbol{x} + r_y\boldsymbol{y} + r_z\boldsymbol{z}$. The path length s can be defined by

$$
\begin{aligned}
&\mathrm{d}s = \sqrt{\mathrm{d}x^2 + \mathrm{d}y^2 + \mathrm{d}z^2}, \quad \left|\frac{\mathrm{d}\boldsymbol{r}}{\mathrm{d}s}\right| = 1,\\
&s = \int \left|\frac{\mathrm{d}\boldsymbol{r}}{\mathrm{d}s}\right| \mathrm{d}s = \int \mathrm{d}s.
\end{aligned} \tag{3}
$$

The geometry meaning of unit vectors $\boldsymbol{\beta}, \boldsymbol{\gamma}, \boldsymbol{\alpha}$ are the curve's normal, bi-normal, and tangent, respectively,[10] where

$$
\boldsymbol{\alpha} = \frac{\mathrm{d}\boldsymbol{r}}{\mathrm{d}s} \Big/ \left|\frac{\mathrm{d}\boldsymbol{r}}{\mathrm{d}s}\right| = \frac{\mathrm{d}\boldsymbol{r}}{\mathrm{d}s}, \quad \boldsymbol{\beta} = \frac{\mathrm{d}\boldsymbol{\alpha}}{\mathrm{d}s} \Big/ \left|\frac{\mathrm{d}\boldsymbol{\alpha}}{\mathrm{d}s}\right|, \quad \boldsymbol{\gamma} = \boldsymbol{\alpha} \times \boldsymbol{\beta}, \tag{4}
$$

The moving unit vectors $(\boldsymbol{\alpha}, \boldsymbol{\beta}, \boldsymbol{\gamma})$ satisfy the Frenet equations

$$
\frac{\mathrm{d}\boldsymbol{\alpha}}{\mathrm{d}s} = \kappa(s)\boldsymbol{\beta}, \quad \frac{\mathrm{d}\boldsymbol{\beta}}{\mathrm{d}s} = -\kappa(s)\boldsymbol{\alpha} + \tau(s)\boldsymbol{\gamma}, \quad \frac{\mathrm{d}\boldsymbol{\gamma}}{\mathrm{d}s} = -\tau(s)\boldsymbol{\beta}, \tag{5}
$$

where $\kappa(s)$ and $\tau(s)$ are the curvature and the torsion of the curve, respectively.

In the static coordinate system, when curved path winding around the spiral body, Eq. (1) takes the following form:

$$
\begin{aligned}
&\boldsymbol{r} = (a(\theta)\cos[f(\theta)], a(\theta)\sin[f(\theta)], b\theta),\\
&s = \int_0^\theta \left|\frac{\mathrm{d}\boldsymbol{r}}{\mathrm{d}\theta}\right| \mathrm{d}\theta\\
&\quad = \int_0^\theta \left|\sqrt{\left(\frac{\mathrm{d}a(\theta)\cos[f(\theta)]}{\mathrm{d}\theta}\right)^2 + \left(\frac{\mathrm{d}a(\theta)\sin[f(\theta)]}{\mathrm{d}\theta}\right)^2 + b^2}\right| \mathrm{d}\theta.
\end{aligned} \tag{6}
$$

According to Eqs. (4) and (5) and Ref. [10], we have

$$
\begin{aligned}
&\boldsymbol{r}' = \frac{\mathrm{d}s}{\mathrm{d}\theta}, \quad \boldsymbol{r}'' = \frac{\mathrm{d}^2 s}{\mathrm{d}\theta^2}, \quad \boldsymbol{r}''' = \frac{\mathrm{d}^3 s}{\mathrm{d}\theta^3},\\
&\kappa = \frac{|\boldsymbol{r}' \times \boldsymbol{r}''|}{|\boldsymbol{r}'|^3}, \quad \tau = \frac{(\boldsymbol{r}' \cdot \boldsymbol{r}'' \cdot \boldsymbol{r}''')}{|\boldsymbol{r}' \times \boldsymbol{r}''|^2}, \quad \boldsymbol{\alpha} = \frac{\boldsymbol{r}'}{|\boldsymbol{r}'|},\\
&\boldsymbol{\beta} = \frac{(\boldsymbol{r}' \cdot \boldsymbol{r}')\boldsymbol{r}'' - (\boldsymbol{r}' \cdot \boldsymbol{r}'')\boldsymbol{r}'}{|\boldsymbol{r}'|\,|\boldsymbol{r}' \times \boldsymbol{r}''|}, \quad \boldsymbol{\gamma} = \frac{\boldsymbol{r}' \times \boldsymbol{r}''}{|\boldsymbol{r}' \times \boldsymbol{r}''|}.
\end{aligned} \tag{7}
$$

Using Eqs. (6) and (7), we can calculate the moving unit vec-

tors $(\boldsymbol{\alpha},\boldsymbol{\beta},\boldsymbol{\gamma})$, and scalar κ and τ as a function of θ as

$$\begin{aligned}&\boldsymbol{\alpha}=\alpha_x\boldsymbol{x}+\alpha_y\boldsymbol{y}+\alpha_z\boldsymbol{z},\quad \boldsymbol{\beta}=\beta_x\boldsymbol{x}+\beta_y\boldsymbol{y}+\beta_z\boldsymbol{z},\\&\boldsymbol{\gamma}=\gamma_x\boldsymbol{x}+\gamma_y\boldsymbol{y}+\gamma_z\boldsymbol{z},\quad \kappa=\kappa(\theta),\quad \tau=\tau(\theta).\end{aligned}\tag{8}$$

Using Eq. (8), it is convenient to transfer Eq. (1) from the static coordinate system to the flowing coordinate system

$$\begin{aligned}\boldsymbol{r}&=a(\theta)\cos[f(\theta)]\boldsymbol{x}+a(\theta)\sin[f(\theta)]\boldsymbol{y}+b\theta\boldsymbol{z},\\&=r_x\boldsymbol{x}+r_y\boldsymbol{y}+r_z\boldsymbol{z}=r_\beta\boldsymbol{\beta}+r_\gamma\boldsymbol{\gamma}+r_\alpha\boldsymbol{\alpha}=\xi\boldsymbol{\beta}+\eta\boldsymbol{\gamma}+\zeta\boldsymbol{\alpha},\\r_\alpha&=\zeta=\boldsymbol{r}\cdot\boldsymbol{\alpha}=r_x\alpha_x+r_y\alpha_y+r_z\alpha_z,\\r_\beta&=\xi=\boldsymbol{r}\cdot\boldsymbol{\beta}=r_x\beta_x+r_y\beta_y+r_z\beta_z,\\r_\gamma&=\eta=\boldsymbol{r}\cdot\boldsymbol{\eta}=r_x\eta_x+r_y\eta_y+r_z\eta_z.\end{aligned}\tag{9}$$

Using Eq. (9), we can easily calculate the photon OAM of a geometric ray along the spiral curve, and the photon OAM is based on the particle property, while the traditional LG OAM is based on the wave property. The only way to connect the photon OAM with the LG OAM is using the Einstein's photon momentum assumption $m\mathrm{d}s/\mathrm{d}t=\hbar k$ to have

$$\boldsymbol{L}=\boldsymbol{r}\times\boldsymbol{p}=\boldsymbol{r}\times m\frac{\mathrm{d}s}{\mathrm{d}t}\frac{\mathrm{d}}{\mathrm{d}s}\boldsymbol{r}=\boldsymbol{r}\times\hbar k\frac{\mathrm{d}}{\mathrm{d}s}\boldsymbol{r}.\tag{10}$$

Thus, we can obtain the OAM of principal ray in units of $\hbar$ in the wave picture

$$\begin{aligned}\boldsymbol{L}/\hbar&=k\boldsymbol{r}\times\frac{\mathrm{d}\boldsymbol{r}}{\mathrm{d}s}\\&=k(r_\alpha\boldsymbol{\alpha}+r_\beta\boldsymbol{\beta}+r_\gamma\boldsymbol{\gamma})\times\frac{\mathrm{d}}{\mathrm{d}s}(r_\alpha\boldsymbol{\alpha}+r_\beta\boldsymbol{\beta}+r_\gamma\boldsymbol{\gamma}).\end{aligned}\tag{11}$$

After a lengthy calculation (see Appendix A), the OAM $\boldsymbol{L}/\hbar$ can be expressed as

$$\boldsymbol{L}/\hbar=\boldsymbol{L}_\alpha/\hbar+\boldsymbol{L}_\beta/\hbar+\boldsymbol{L}_\gamma/\hbar,\tag{12}$$

where $\boldsymbol{L}_\alpha/\hbar$ is the OAM along the tangential direction $\boldsymbol{\alpha}$, namely, the direction of the principal ray. $\boldsymbol{L}_\alpha/\hbar$ is composed of two parts $\boldsymbol{L}_\alpha/\hbar=\boldsymbol{L}_{\alpha1}/\hbar+\boldsymbol{L}_{\alpha2}/\hbar$, where

$$\begin{aligned}\boldsymbol{L}_{\alpha1}/\hbar&=\left(r_\beta\frac{\mathrm{d}r_\gamma}{\mathrm{d}s}-r_\gamma\frac{\mathrm{d}r_\beta}{\mathrm{d}s}\right)\boldsymbol{\alpha},\\\boldsymbol{L}_{\alpha2}/\hbar&=(r_\gamma r_\gamma\tau-r_\gamma r_\alpha\kappa+r_\beta r_\beta\tau)\boldsymbol{\alpha}.\end{aligned}\tag{13}$$

In the flowing coordinate system, the wave inside the fiber satisfies the equation of $u(\xi,\eta,\zeta,t)$, and

$$\begin{aligned}&\frac{1}{\rho}\frac{\partial}{\partial\rho}\left(\rho\frac{\partial u}{\partial\rho}\right)+\frac{1}{\rho^2}\frac{\partial^2u}{\partial\varphi^2}+\frac{\partial^2u}{\partial\zeta^2}-\frac{1}{c^2}\frac{\partial^2u}{\partial t^2}=0,\\&\rho=\sqrt{\xi^2+\eta^2},\quad\varphi=\tan^{-1}\left[\frac{\xi}{\eta}\right].\end{aligned}\tag{14}$$

Substituting u in Eq. (12), we have

$$\begin{aligned}&u=y(\rho)\mathrm{e}^{-\mathrm{i}\nu\varphi}\mathrm{e}^{-\mathrm{i}(\omega t-k_\zeta\zeta)}=y(\rho)\mathrm{e}^{-\mathrm{i}\nu\varphi}\mathrm{e}^{-\mathrm{i}\theta_l},\\&\boldsymbol{L}_\alpha/\hbar u=\mathrm{i}\frac{\partial}{\partial\varphi}u=\nu u,\end{aligned}\tag{15}$$

$$\frac{1}{\rho}\frac{\partial}{\partial\rho}\left(\rho\frac{\partial y}{\partial\rho}\right)+\left(k^2-\frac{\nu^2}{\rho^2}\right)y=0,\quad k^2=\frac{\omega^2}{c^2}-k_\zeta^2,\tag{16}$$

where u satisfies the boundary condition $|u|=0$, when $\rho\geq\rho_0$, where ρ_0 is the optical fiber radius. The solution of $y(\rho)$ can be written in terms of the Bessel function of ρ/ρ_0 as

$$y(\rho)=J_\nu\left(s_{\nu n}\frac{\rho}{\rho_0}\right),\quad y(\rho_0)=J_\nu(s_{\nu n})=0.\tag{17}$$

The OAM ν can be expressed by the relation $L_\alpha/\hbar u=\mathrm{i}u\partial u/\partial\varphi=\nu u$.[11] $s_{\nu n}$ are the n-th roots of Bessel function with OAM, which guarantees the boundary condition of u satisfied. Due to the requirement of optical fiber inner total reflection, the roots of Bessel function must satisfy the inequality $s_{\nu n}\leq 2\pi\rho_0\sqrt{n_1^2-n_2^2}/\lambda$, where λ, n_1, and n_2 are the laser wave length, the optical fiber's inner refraction index for $\rho<\rho_0$, and the optical fiber's outside refraction index for $\rho>\rho_0$, respectively. We can calculate the diffraction pattern by using the solutions of u (see Appendix B).

4. Numerical calculations of the OAM

Figures 3(a) and 3(b) depict the three dimension spiral path around the "Exponential" curve and $\boldsymbol{L}_\alpha/\hbar$ is a function of θ as shown in Figs. 3(b1)–3(b3). We can find out:

(i) Homogeneous winding (see Figs. 3(a1)–3(b1)) is uniform, but the spiral path amplitude and $\boldsymbol{L}_\alpha/\hbar$ gradually decrease to zero at the same time, which can not give a large OAM.

(ii) In-homogeneous winding (see Figs. 3(a2)–3(b2)) gradually decreases to a straight line (see Fig. 3(a2)), and the $\boldsymbol{L}_\alpha/\hbar$ curve (see Fig. 3(b2)) drops simultaneously from a high value to a low gradually, which also can not generate a large OAM.

(iii) The two stages winding (see Figs. 3(a3)–3(b3)) consists of two parts. The first homogeneous winding begins from $\theta=0$ to 200, and the $\boldsymbol{L}_\alpha/\hbar$ increases from 0 to 148. The second stopping winding begins from $\theta=200$ to 1000, the $\boldsymbol{L}_\alpha/\hbar$ maintains at 148, and the curve of Figs. 3(a3) moves in the direction of the tangent direction gradually approaching to a straight line. More discussions are given in Section 7.

It is useful for us to obtain a high OAM modes when light beam propagates along a straight line. The continuity of curve at $\theta=200$ will be proved in Appendix C.

From the above we can not come to the conclusion that the spiral path (see Figs. 3(b1) or 3(b2)) is not a valid path to obtain the large OAM modes. Because there are two kinds of optical fiber winding directions, one is the clockwise direction winding from right to left, and the other is the anti-clockwise direction winding from left to right. From the zero OAM increasing to the maximum OAM, we adopt the anti-clockwise direction winding, and after reaching the maximum OAM, we adopt the clockwise direction winding. In the exponential type Eq. (2), the anti-clockwise winding function $f_{\mathrm{c}}(\theta)=\theta/(1+l_2|\theta|)$, and the clockwise winding function $f_{\mathrm{ac}}(\theta)=-\theta/(1+l_2|\theta|)$. The numerical calculations of spiral path according to anti-clockwise direction before the

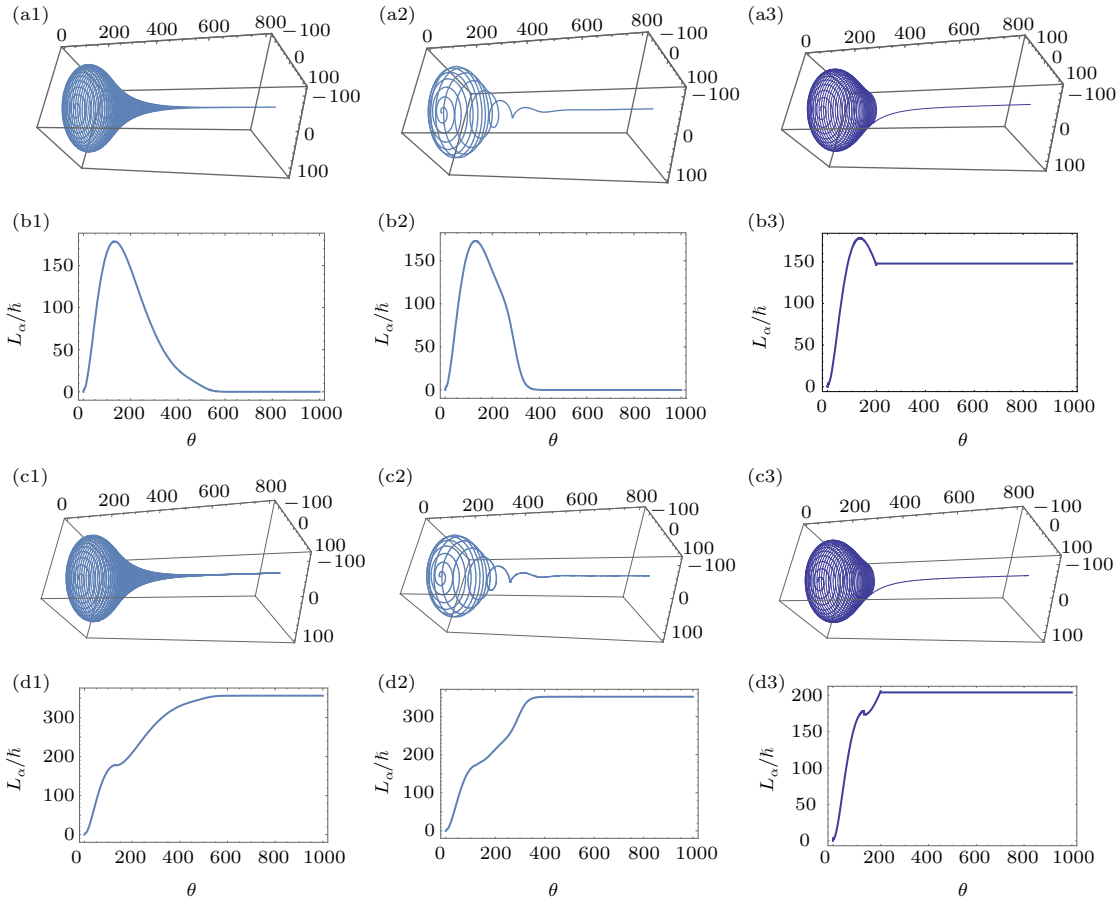


Fig. 3. The three-dimensional spiral path around the exponential type $L_\alpha/\hbar$ as a function of θ with parameters $ka = 5$, $kb = 1$, (a1), (b1) $l_1 = 0.015$, $l_2 = 0$, homogeneous winding; (a2), (b2) $l_1 = 0.015$, $l_2 = 0.01$, in-homogeneous winding; (a3), (b3) $l_1 = 0.015$, $\theta = 0-200$, $l_2 = 0$, homogeneous winding, $\theta = 200$–1000, $l_2 = \infty$, stop-winding. (c1), (c2), (c3) and (d1), (d2), (d3) change the winding direction at the maxima of $L_\alpha/\hbar$.

maximum of $L_\alpha/\hbar$ (the winding function $f_c(\theta)$) and afterward according to clockwise direction (the winding function $f_{ac}(\theta)$) are depicted in Figs. 3(c1)–3(c3), and the corresponding large OAM are shown in Figs. 3(d1)–3(d3), respectively.

In Figs. 4 and 5, we depict the three dimensional spiral curves with $L_\alpha/\hbar$ as a function of θ for the Gaussian and the Flower types, respectively. The winding are homogeneous $l_2 = 0$.

This curve tells us that we can obtain a large OAM modes easily.

One interesting thing is the Flower type OAM with $L_\alpha/\hbar$ as a periodic function of θ, and the maximum and minimum locates nearly at two straight lines $L_\alpha/\hbar \approx \pm 60 \times \theta, \pm 100 \times \theta, \pm 250 \times \theta$ for $n = 1, 3, 5$, respectively. The input light beam should be along the tangent direction near the position $\theta \approx 0$ of Figs. 5(b1)–5(b3). Figures 5(a1) and 5(a2) show clearly the low ends of the optical fiber, which is the position of the input beam.

The input light beam should be along the tangent direction near the position $\theta \approx 0$ of Figs. 5(b1)–5(b3). Figures 5(a1) and 5(a2) show that the point $\theta \approx 0$ locates at the milder of the optical fiber. It is a suitable input beam position, due to $\theta \approx 0$, $L_\alpha/\hbar \approx 0$, and $d(L_\alpha/\hbar)/d\theta = 0$. If we choose the end of the optical fiber as the input beam, due to $\theta = -10$, and $L_\alpha/\hbar \neq 0$, we must choose a point near the end and satisfying the condition $L_\alpha = 0$. Refer to Fig. 5, the points of $L_\alpha = 0$ are $\theta = -9.4, -9.9, -9.95$ for $n = 1, 3, 5$, respectively.

For the purpose of convenience of experimental realization, we give some explanations. In Figs. 1–3, the parameter $kb_0 = 1$, yields $r_z = \theta\lambda_0/2\pi$, and $\delta r_z = \delta\theta\lambda_0/2\pi$. When the spiral path makes a circuit, $\delta\theta = 2\pi$, the distance between adjacent spiral coil satisfies $\delta r_z = d = \lambda_0$. Here λ_0 is the orbital wave length. As shown in Fig. 1(b1), we set $d = 0.1$ cm, $\theta = 1000$, then the total length of the spiral body equals to $r_z = 0.16$ m and we have $k_z r_z = \theta\lambda_0/\lambda = \theta d/\lambda$, where λ is the laser wave length. In the flowing coordinate system (see Eq. (15)) $k_z r_z = \theta d/\lambda \to \theta_l = -(\omega t - k_\zeta \zeta)$. In general, the variable θ is essential for the θ_l in the wave function Eq. (16), except a constant factor d/λ.

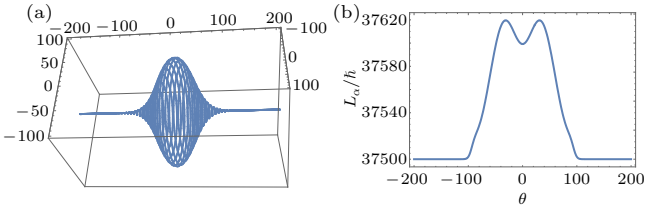


Fig. 4. The Gaussian type with parameters $ka = 100$, $kb = 1$, $l_1 = 0.0005$, $l_2 = 0$: (a) three-dimensional curve, (b) $L_\alpha/\hbar$ as a function of θ.

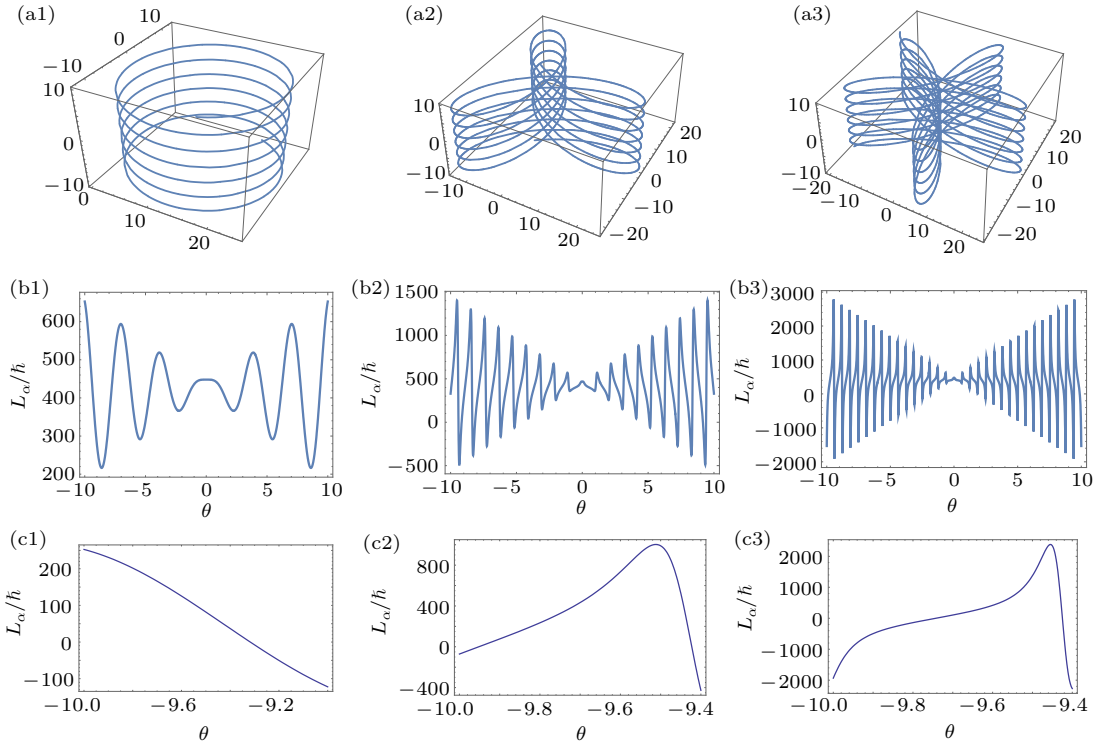


Fig. 5. The flower type with parameters $ka = 25$, $kb = 1$, $l_2 = 0$. (a1) $n = 1$, (a2) $n = 3$, (a3) $n = 5$, three-dimensional curve; (b1) $n = 1$, (b2) $n = 3$, (b3) $n = 5$, $L_\alpha/\hbar$ as a function of θ; (c1) $n = 1$, (c2) $n = 3$, (c3) $n = 5$, the flower type finding zero point curve.

5. Diffraction pattern calculations and applications

Before the diffraction pattern calculations, we need demarcate the diffraction modes in free space and the diffraction modes inside the optical fiber.

According to Eq. (17), s_{00} and s_{016} in Eq. (6) indicate $\nu = 0$ and $n = 0, 16$ for Figs. 6(b1)–6(b2) and 6(c1)–6(c$_2$), respectively. As shown in Figs. 6(a1) and 6(a2), the diffraction pattern represents the Rayleigh criterion of spatial resolving power (see Fig. 8.12 in Ref. [12]), the abscissa of curves in Figs. 6(a1) and 6(a2) are $x_a = k\rho w = k\rho\sqrt{p^2+q^2} = k\rho\sin[\theta]$, where θ is the diffraction angle between the diffraction direction and the principal ray, and ρ denotes the radius of circular. The abscissa of Figs. 6(b1)–6(b2) and 6(c1)–6(c$_2$) have the same definition as Figs. 6(a1)–6(a2), $x_b = x_c = k\rho w = k\rho\sqrt{p^2+q^2}$, although the magnitude are quite different. The maximum intensity are 10, 34, and 730 for Figs. 6(a1), Fig. 6(b1), and Fig. 6(c1), respectively. The zero intensity locates at 3.83, 1.8, and 0.08 for Figs. 6(a1), 6(b1), and 6(c1), respectively. The total energy enclosed in the diffraction patterns can be estimated by $10 \times 3.83^2 = 146$, $34 \times 1.8^2 = 110$, and $730 \times 0.08^2 = 4.67$, for Figs. 6(a2), 6(b2), and 6(c2), respectively. The important thing is the zero intensity location determines spatial resolving power limit. For convenience, we take the Rayleigh criterion zero intensity location 3.83 as resolving power unit, and the relative resolving power for Figs. 6(b1) and 6(c1) is $3.83/1.8 = 2.13$ and $3.83/0.08 = 47.9$, which come close to $s_{00} = 2.3$, and $s_{016} = 49.5$, respectively.

The underlying physics meaning will be discussed in Section 7.

With the purpose of observation of the diffraction patterns calculated in Fig. 3(b1), the OAM region $\nu = 0$–53 as shown in Table 1.

The first group contains a_1–a_{12} diffraction patterns for $\theta = 0$–24 and $\nu = 0$–30 (see Table 1), and the second group contains b_1–b_{12} diffraction patterns for $\theta = 29$–34.5 and $\nu = 42$–53 (see Table 1).

For simplification, the diffraction patterns shown in Figs. 7(a) and 7(b) present only part of that listed in Table 1.

By utilizing the 12-bit (a_i, b_i, $i = 1$–12) encoded diffraction patterns and the experimental observation of the OAM as a function of time (the temporal variation of diffraction patterns), the optical information transfer may be realized in principle. Combining the total 24 patterns, we have more different 12-bit encodes.

Table 1. The a_1–a_{12} diffraction patterns for $\theta = 0$–24 and $\nu = 0$–30, the b_1–b_{12} diffraction patterns for $\theta = 29$–34.5 and $\nu = 42$–53.

a	a_1	a_2	a_3	a_4	a_5	a_6	a_7	a_8	a_9	a_{10}	a_{11}	a_{12}
θ	0	2	4	6	8	10	12	14	16	18	20	24
ν	0	2.54	3.42	4.2	5.42	7.40	9.52	15.52	15	18	22.2	30
$s_{\nu 0}$	2.3	5.75	6.9	7.9	9.2	11.5	14	17.5	20	23	28	36
b	b_1	b_2	b_3	b_4	b_5	b_6	b_7	b_8	b_9	b_{10}	b_{11}	b_{12}
θ	29	29.5	30	31.2	31.8	32.1	32.4	32.8	33.2	33.5	34	34.5
ν	42	43	44	45	46	47	48	49	50	$_{51}$	52	53
$s_{\nu 0}$	48.7	49.7	50.9	52	53	54	55	56.2	57	58.2	59	60.4

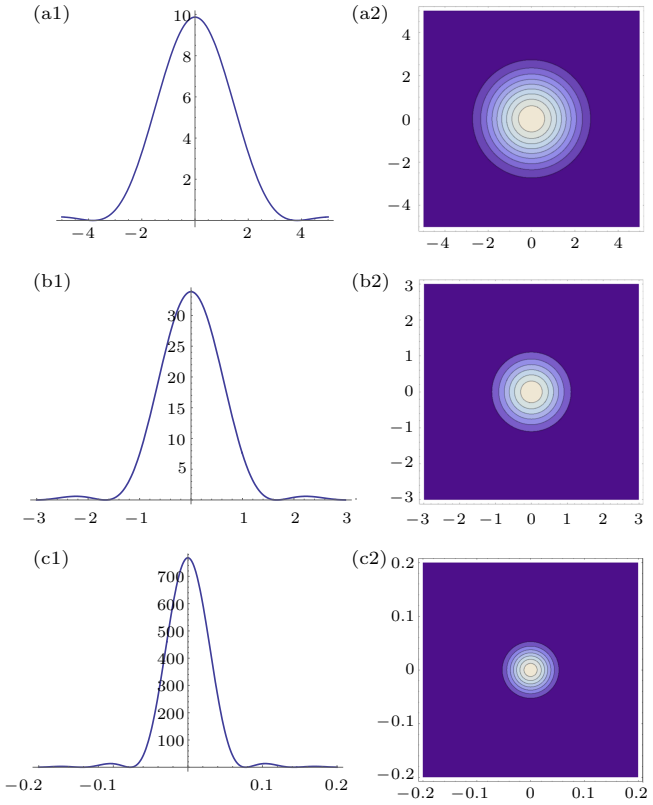


Fig. 6. (a1)–(a2) The diffraction pattern in free space $v = L_\alpha/\hbar = 0$;[12] (b1)–(b2) inside the optical fiber (see Appendix B) $v = L_\alpha/\hbar = 0$, $s_{00} = 2.3$; (c1)–(c$_2$) inside the optical fiber $s_{016} = 49.5$.

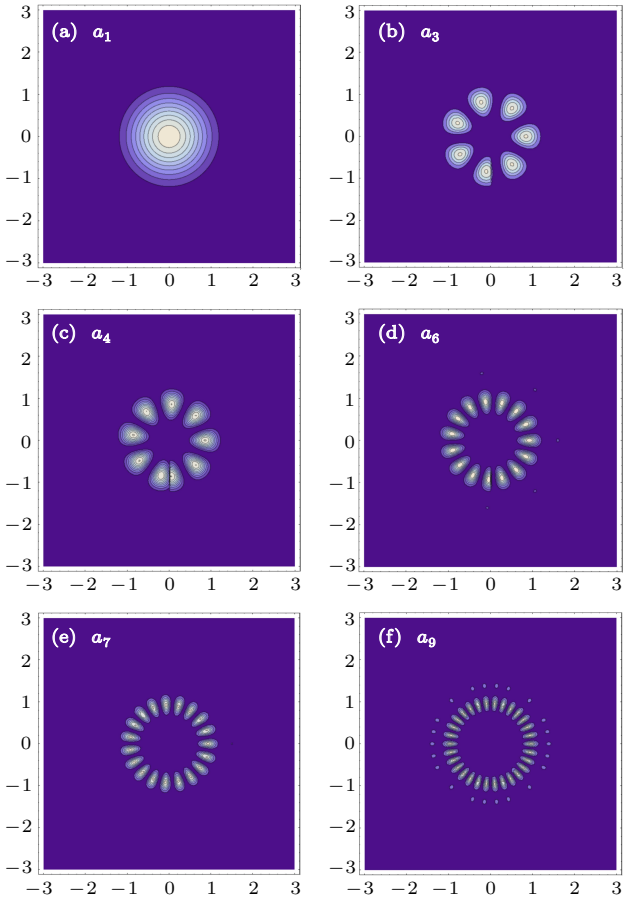


Fig. 7(a). Part of the a_1–a_{12} diffraction patterns (listed in Table 1) of optical fiber at the end of spiral body in Fig. 3(b1).

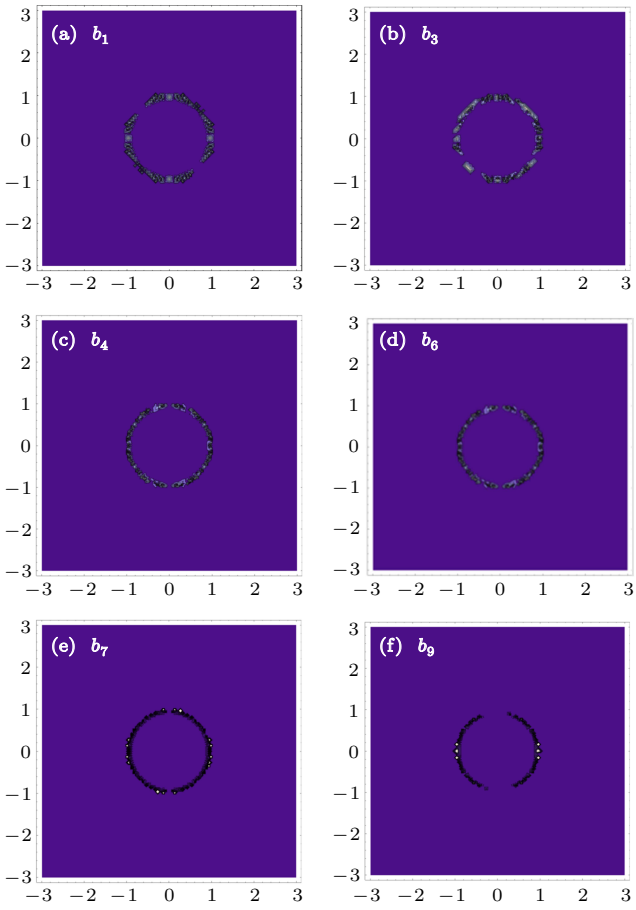


Fig. 7(b). Part of the b_1–b_{12} diffraction patterns (listed in Table 1) of optical fiber at the end of spiral body in Fig. 3(b1).

6. A thinking experimental scheme for observation of a large OAM temporal pulse

The diffraction patterns calculated in Figs. 6 and 7 are electric fields inside the optical fiber, which can not be observed directly. In order to observe these patterns, we must let it propagate out of the fiber and transfer a distance z arriving the screen. For this purpose and refer to Ref. [14], we propose a thinking experimental scheme for observation of a large OAM temporal pulse as shown in Fig. 8, using the linear polarized laser as the input beam.

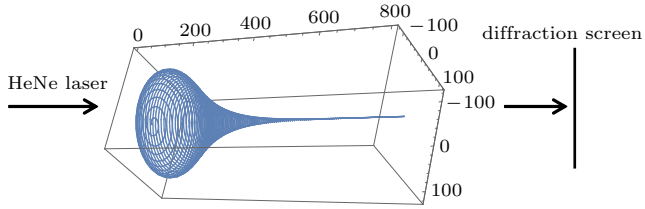


Fig. 8. The optical fiber winding is stopped at $\theta_0 = 388$, $v = 30$, $z = B = 0.07$ m, 0.7 m.

The electric field of laser beam is incident from the left-side of circular cone enjoying the form $E^0(r,\theta) = A_0\,\mathrm{e}^{-r^2/w^2}$, and after passing through the spiral curve winding the circular cone (see Fig. 3(b3), the homogenous winding $\theta = 0$–θ_0, and the stop winding $\theta > \theta_0$), the electric field of large OAM spiral

optical fiber (SOF) $E^0_{\rm sof}(r,\theta)$ presents at the end of right-side of circular cone, then transfers z distance in free space to arrive the screen. We can calculate the diffraction patterns with the help of Collins formula[15]

$$E_{\rm sof}(\rho,r,\theta)=\frac{{\rm i}kA_0}{2kB}{\rm e}^{-\frac{{\rm i}kD\rho^3}{2B}}\times\int_0^{\infty}\int_0^{2\pi}E^0_{\rm sof}(r,\theta){\rm e}^{-\frac{{\rm i}kAr^2}{2B}}{\rm e}^{-\frac{{\rm i}k\rho r}{B}\cos[\theta-\varphi]}r{\rm d}r{\rm d}\varphi. \quad (18)$$

In real calculation, we take $E^0_{\rm sof}(r,\theta)=a_9,a_{12}$ in Fig. 7(a). The parameters are listed in Table 2.

We can observe the following diffraction pattern in Fig. 7(a).

Table 2. The parameters of the electric field of large OAM spiral optical fiber $E^0_{\rm sof}(r,\theta)=a_9,a_{12}$ in Fig. 7(a) with the same ν and z.

a	a_9	a_9	a_{12}	a_{12}
θ	16	16	24	24
ν	15	15	30	30
s_ν	20	20	36	36
z/m	0.07	0.7	0.07	0.7

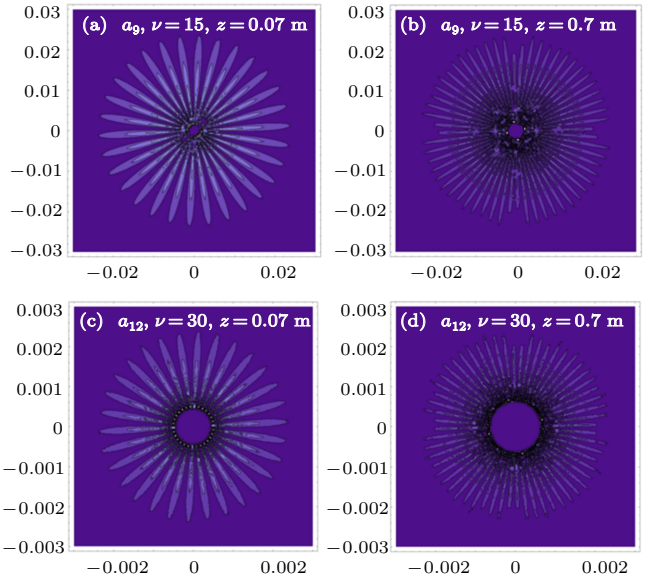


Fig. 9. The spiral optical fiber (SOF) modes a_9, a_{12} (see Fig. 7) propagate through a distance $z=0.07$ m, $z=0.7$ m and arrive at the diffraction screen, where ν denotes the OAM modes.

For reference, we remove the circular cone from Fig. 8 and let the laser beam incident directly to the diffraction screen with the same ν and z, and the traditional circular hole (CIH) diffraction patterns are also calculated

$$E_{\rm cih}(\rho,r,\theta)=\frac{{\rm i}kA_0}{2kB}{\rm e}^{-\frac{{\rm i}kD\rho^3}{2B}}\times\int_0^{\infty}\int_0^{2\pi}E^0_{\rm cih}(r,\theta){\rm e}^{-\frac{{\rm i}kAr^2}{2B}}{\rm e}^{-\frac{{\rm i}k\rho r}{B}\cos[\theta-\varphi]}r{\rm d}r{\rm d}\varphi,$$
$$E^0_{\rm cih}(r,\theta)=A_0{\rm e}^{-r^2/w^2}{\rm e}^{-{\rm i}\nu\theta},\quad \nu=L_\alpha/\hbar,$$
$$w(z)=w_0\sqrt{1+(\lambda z/\pi w_0^2)^2}. \quad (19)$$

According to Ref. [16], the beam spot size $w(z)$, the radius of optical fiber ρ_0, the minimum beam spot size $w(0)=w_0=\rho_0=s_{\nu 0}/k$. The diffraction patterns $E_{\rm sof}(\rho,r,\theta)$, and $E_{\rm cih}(\rho,r,\theta)$ on the screen are calculated as shown in Figs. 9, and 10, respectively. The SOF and CIH diffraction patterns present a quit different intensity distribution on the screen when we take the same ν and z.

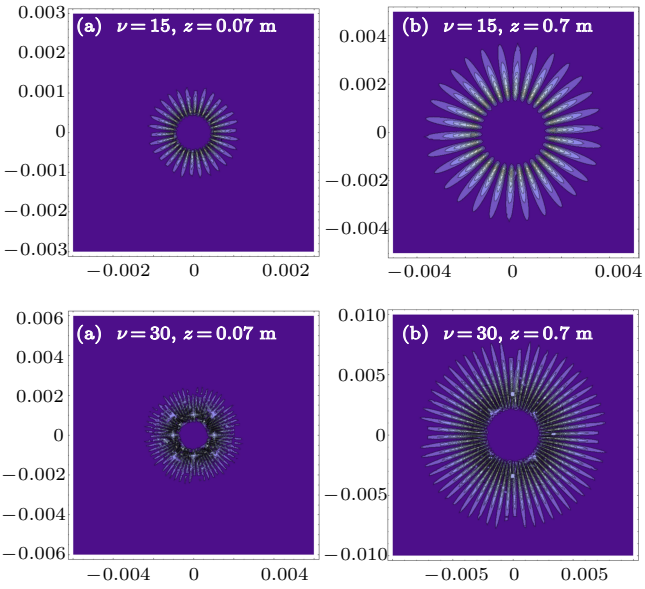


Fig. 10. The circular hole (CIH) modes propagate through a distance $z=0.07$ m, $z=0.7$ m and arrive at the diffraction screen, where ν denotes the OAM modes.

7. Discussion and conclusion

In this paper, based on the differential Frenet equation and Einstein's photon momentum assumption, we obtain an analytical solution for the OAM of ray propagating in an optical fiber with winding around a spiral body, then we proceed the numerical calculations of the OAM of the principal light and the diffraction patterns at different point θ corresponding to different OAM. The diagrams of OAM depicted in Figs. 3(b1)–3(b3) demonstrate that the necessary and sufficient conditions for an increase (or decrease) of $\delta(L_\alpha/\hbar)\neq 0$, are $a(\theta)>0$ and winding $\delta\theta\neq 0$. In Figs. 3(b1) and 3(b2), we find out that when $a(\theta)\to 0$, $\delta(L_\alpha/\hbar)\to 0$. In Fig. 3(b3), the winding stop point at $\theta=200$, $L_\alpha/\hbar$=148. when $\theta>200$, $\delta(L_\alpha/\hbar)=0$. In theory,[10] it is proved when curvature $\kappa(\theta)=0$, the curve degenerates to a straight line; when torsion $\tau(\theta)=0$, the curve is a plane curve; the necessary and sufficient condition of the curve being space curve is $\kappa(\theta)\neq 0$, and $\tau(\theta)\neq 0$. The second stopping winding stage of Fig. 3(a3) shows the path of fiber is a plane curve, the torsion $\tau(\theta)=0$, a simple algebra also giving $r_\gamma=r_x\eta_x+r_y\eta_y+r_z\eta_z=0$, and using Eq. (13), it is easily to prove $L_{\alpha 1}/\hbar=L_{\alpha 2}/\hbar=0$. This means in the second stage, there is no new contribution to the total OAM.

The results in Figs. 3(c1)–3(c3) and 3(d1)–3(d3) supplement that of Figs. 3(a1)–3(a3) and 3(b1)–3(b3) by changing the winding direction from clockwise to anti-clockwise at the maxima of $L_\alpha/\hbar$, with the OAM maintaining a high vale , and

the circular-cone approaching a straight line, in the limit of $\theta \to \infty$.

The calculated diffraction patterns provide a 12 bit OAM-encoded ultrahigh-security information system. From the viewpoint of fundamental research, the OAM of principal ray winding around a spiral curve is a particle picture, while the OAM of LG beam is a wave picture. The connection between the two pictures is the Einstein's assumption for the photon momentum $m\mathrm{d}s/\mathrm{d}t = \hbar k$. In the theoretical study of spiral curves, it includs "Exponential", "Gaussian", and "Flower" types, while in reality, the first and second type are easily to obtain a high OAM up to 10^{3-5}, and the third "Flower" type is very interesting, which has a periodic relation between the maximum and minimum of OAM output.

In the calculation of the diffraction pattern, due to the boundary condition Eq. (17), the wave modes SOF propagating inside the optical fiber have a higher space resolving power limiting than the CIH mode's Rayleigh limiting. This result seems to violate the uncertainty principle $\Delta p_x \Delta x \geq \hbar$ in quantum mechanics.[11] We also know the Rayleigh spatial resolving limiting experiment leads to single-photon uncertainty principle $\Delta p_x \Delta x \geq \hbar$. In the case of multi-photon experiment, a high spatial resolving limiting $\Delta x/n$ naturally yields from the multi-photon uncertainty principle $(n\Delta p_x)(\Delta x/n) \geq \hbar$, where n is the photon number. The optical fiber plays an important role in the selection of the multi-photon modes s_{0n}, which satisfies the boundary condition $s_{0n} = k\rho_0$ and the total internal reflection $s_{0n} \leq 2\pi\rho_0\sqrt{n_1^2 - n_2^2}/\lambda$. Figures 6(b1)–6(c1) show the spatial resolving power $s_{00} = 2.3$, and $s_{016} = 49.5$ in units of Rayleigh limiting, and the total energy reduced. A full description of the laser photon distribution is beyond the scope of this paper.

Appendix A: OAM calculation

$$
\begin{aligned}
\boldsymbol{L}/\hbar &= \boldsymbol{r} \times k\frac{\mathrm{d}\boldsymbol{r}}{\mathrm{d}s} \\
&= (r_\alpha\boldsymbol{\alpha} + r_\beta\boldsymbol{\beta} + r_\gamma\boldsymbol{\gamma}) \times k\frac{\mathrm{d}}{\mathrm{d}s}(r_\alpha\boldsymbol{\alpha} + r_\beta\boldsymbol{\beta} + r_\gamma\boldsymbol{\gamma}) \\
&= (r_\alpha\boldsymbol{\alpha} + r_\beta\boldsymbol{\beta} + r_\gamma\boldsymbol{\gamma}) \times k\left(\frac{\mathrm{d}r_\alpha}{\mathrm{d}s}\boldsymbol{\alpha} + \frac{\mathrm{d}r_\beta}{\mathrm{d}s}\boldsymbol{\beta} + \frac{\mathrm{d}r_\gamma}{\mathrm{d}s}\boldsymbol{\gamma}\right. \\
&\quad \left. + r_\alpha\frac{\mathrm{d}\boldsymbol{\alpha}}{\mathrm{d}s} + r_\beta\frac{\mathrm{d}\boldsymbol{\beta}}{\mathrm{d}s} + r_\gamma\frac{\mathrm{d}\boldsymbol{\gamma}}{\mathrm{d}s}\right) \\
&= (r_\alpha\boldsymbol{\alpha} + r_\beta\boldsymbol{\beta} + r_\gamma\boldsymbol{\gamma}) \times k\left[\frac{\mathrm{d}r_\alpha}{\mathrm{d}s}\boldsymbol{\alpha} + \frac{\mathrm{d}r_\beta}{\mathrm{d}s}\boldsymbol{\beta} + \frac{\mathrm{d}r_\gamma}{\mathrm{d}s}\boldsymbol{\gamma}\right. \\
&\quad \left. + r_\alpha(\kappa\boldsymbol{\beta}) + r_\beta(-\kappa\boldsymbol{\alpha} + \tau\boldsymbol{\gamma}) + r_\gamma(-\tau\boldsymbol{\beta})\right] \\
&= (r_\alpha\boldsymbol{\alpha} + r_\beta\boldsymbol{\beta} + r_\gamma\boldsymbol{\gamma}) \times k\left[\left(\frac{\mathrm{d}r_\alpha}{\mathrm{d}s} - r_\beta\kappa\right)\boldsymbol{\alpha}\right. \\
&\quad \left. + \left(\frac{\mathrm{d}r_\beta}{\mathrm{d}s} + r_\alpha\kappa - r_\gamma\tau\right)\boldsymbol{\beta} + \left(\frac{\mathrm{d}r_\gamma}{\mathrm{d}s} + r_\beta\tau\right)\boldsymbol{\gamma}\right] \\
&= kr_\alpha\boldsymbol{\alpha} \times \left[\left(\frac{\mathrm{d}r_\beta}{\mathrm{d}s} + r_\alpha\kappa - r_\gamma\tau\right)\boldsymbol{\beta} + \left(\frac{\mathrm{d}r_\gamma}{\mathrm{d}s} + r_\beta\tau\right)\boldsymbol{\gamma}\right] \\
&\quad + kr_\beta\boldsymbol{\beta} \times \left[\left(\frac{\mathrm{d}r_\alpha}{\mathrm{d}s} - r_\beta\kappa\right)\boldsymbol{\alpha} + \left(\frac{\mathrm{d}r_\gamma}{\mathrm{d}s} + r_\beta\tau\right)\boldsymbol{\gamma}\right] \\
&\quad + kr_\gamma\boldsymbol{\gamma} \left[\left(\frac{\mathrm{d}r_\alpha}{\mathrm{d}s} - r_\beta\kappa\right)\boldsymbol{\alpha} + \left(\frac{\mathrm{d}r_\beta}{\mathrm{d}s} + r_\alpha\kappa - r_\gamma\tau\right)\boldsymbol{\beta}\right] \\
&= \boldsymbol{L}_\alpha/\hbar + \boldsymbol{L}_\beta/\hbar + \boldsymbol{L}_\gamma/\hbar,
\end{aligned}
$$

where

$$
\begin{aligned}
\boldsymbol{L}_\alpha/\hbar &= k\left[r_\beta\left(\frac{\mathrm{d}r_\gamma}{\mathrm{d}s} + r_\beta\tau\right) - r_\gamma\left(\frac{\mathrm{d}r_\beta}{\mathrm{d}s} + r_\alpha\kappa - r_\gamma\tau\right)\right]\boldsymbol{\alpha}, \\
\boldsymbol{L}_\beta/\hbar &= k\left[-r_\alpha\left(\frac{\mathrm{d}r_\gamma}{\mathrm{d}s} + r_\beta\tau\right) + r_\gamma\left(\frac{\mathrm{d}r_\alpha}{\mathrm{d}s} - r_\beta\kappa\right)\right]\boldsymbol{\beta}, \\
\boldsymbol{L}_\gamma/\hbar &= k\left[r_\alpha\left(\frac{\mathrm{d}r_\beta}{\mathrm{d}s} + r_\alpha\kappa - r_\gamma\tau\right) - r_\beta\left(\frac{\mathrm{d}r_\alpha}{\mathrm{d}s} - r_\beta\kappa\right)\right]\boldsymbol{\gamma}. \qquad \text{(A1)}
\end{aligned}
$$

Appendix B: Diffraction pattern integral

Using the solutions u, the diffraction pattern can be calculated. Similar to the

Rayleigh criterion calculation,[11] where diffraction integral is expressed as $U(P) = 2\pi C\int_0^a J_0(k\rho w)\rho\,\mathrm{d}\rho$.

In the case of OAM $\nu \neq 0$, the diffraction integral[12]

$$
\begin{aligned}
U(P) &= 2\pi C\mathrm{i}^\nu \int_0^a J_\nu(k\rho w)\cos\left[\nu\tan^{-1}\left[\frac{y}{x}\right]\right]\rho\,\mathrm{d}\rho \\
&= 2\pi\mathrm{i}^\nu C\rho_0^2\int_0^1 J_\nu(s_{\nu n}rw)\cos\left[\nu\tan^{-1}\left[\frac{y}{x}\right]\right]r\,\mathrm{d}r, \\
s_{\nu n} &= k\rho_0, \quad r = \frac{\rho}{\rho_0}, \quad J_\nu(s_{\nu n}) = 0, \quad w = \sqrt{x^2+y^2}, \\
\varphi_\nu(s_{\nu n}rw) &= \frac{J_\nu(s_{\nu n}rw)}{J'_\nu(s_{\nu n})}, \\
J'_\nu(s_{\nu n}) &= \frac{\mathrm{d}J'_\nu(z)}{\mathrm{d}z}|_{z=s_{\nu n}} = \frac{J_{\nu-1}(s_{\nu n}) - J_{\nu+1}(s_{\nu n})}{2}, \qquad \text{(B1)} \\
|U(P)|^2 &= \left(\int_0^1 \varphi_\nu(s_{\nu n}rw)\cos\left[\nu\tan^{-1}\left[\frac{y}{x}\right]\right]r\,\mathrm{d}r\right)^2 I_0, \qquad \text{(B2)}
\end{aligned}
$$

where $\varphi_\nu(s_{\nu n}rw)$ is the normalized wave function,[17] the last integral in Eqs. (B1) and (B2) are used in the diffraction pattern's calculation.

Appendix C: The proof of curve continue of Fig. 3(b3)

In mechanics, the OAM can be expressed as the integral of the torque $\boldsymbol{T} = \boldsymbol{r} \times \boldsymbol{F}$ due to the force $\boldsymbol{F}$ acting on the moving particles.[18] According to Eq. (10)

$$
\begin{aligned}
\boldsymbol{L} &= \boldsymbol{r} \times \boldsymbol{p} = \int_0^t \frac{\mathrm{d}}{\mathrm{d}t}\left(\boldsymbol{r} \times m\frac{\mathrm{d}\boldsymbol{r}}{\mathrm{d}t}\right)\mathrm{d}t \\
&= \int_0^t \boldsymbol{r} \times m\frac{\mathrm{d}^2\boldsymbol{r}}{\mathrm{d}t^2}\mathrm{d}t = \int_0^t \boldsymbol{r} \times \boldsymbol{F}\,\mathrm{d}t \\
&= \int_0^{\theta_0-\varepsilon} \boldsymbol{r} \times \boldsymbol{F}_1\,\mathrm{d}\theta\,\omega^{-1}
\end{aligned}
$$

$$
\begin{aligned}
&+\int_{\theta_0-\varepsilon}^{\theta_0+\varepsilon} \boldsymbol{r}\times\left(\frac{\boldsymbol{F}_1+\boldsymbol{F}_2}{2}+\frac{\boldsymbol{F}_1-\boldsymbol{F}_2}{2}\mathrm{Sgn}[\theta-\theta_0]\right)\mathrm{d}\theta\omega^{-1}\\
&+\int_{\theta_0+\varepsilon}^{\theta} \boldsymbol{r}\times\boldsymbol{F}_2\,\mathrm{d}\theta\omega^{-1}\\
=&\int_{0}^{\theta_0-\varepsilon} \boldsymbol{r}\times\boldsymbol{F}_1\,\mathrm{d}\theta\omega^{-1}\\
&+\varepsilon\boldsymbol{r}\times((\boldsymbol{F}_1+\boldsymbol{F}_2)+(\boldsymbol{F}_1-\boldsymbol{F}_2)\mathrm{Sgn}[\theta-\theta_0])\omega^{-1}\\
&+\int_{\theta_0+\varepsilon}^{\theta} \boldsymbol{r}\times\boldsymbol{F}_2\,\mathrm{d}\theta\omega^{-1},
\end{aligned}
\tag{C1}
$$

where the acting forces F_1, and F_2 present the acting forces of the homogeneous winding stage and the stopping winding stage. Eq. (C1) shows that OAM L seems discontinuous due to the term $\varepsilon\boldsymbol{r}\times((\boldsymbol{F}_1+\boldsymbol{F}_2)+(\boldsymbol{F}_1-\boldsymbol{F}_2)\mathrm{Sgn}[\theta-\theta_0])\omega^{-1}$, but in the limit $\varepsilon\to 0$, and the acting force of the stopping winding stage $\boldsymbol{F}_2=0$, therefore, we have a continuous solution $L/\hbar=\int_0^{\theta_0}\boldsymbol{r}\times\boldsymbol{F}_1\,\mathrm{d}\theta(\hbar\omega)^{-1}$ as a function of θ shown in Fig. 3(b3) ($\theta_0=200$).

References

[1] Courtial J, Dholakia K, Allen L and Padgett M J 1997 *Opt. Commun.* **144** 210

[2] Sundbeck S, Gruzberg I and Grier D G 2005 *Opt. Lett.* **30** 477

[3] Galvez E J, Crawford P R, Sztul H I, Pysher M J, Haglin P J and Williams R E 2003 *Phys. Rev. Lett.* **90** 203901

[4] Savchenkov A A, Matsko A B, Grudinin I, Savchenkova E A, Strekalov D and Maleki L 2006 *Opt. Exp.* **14** 2888

[5] Ramachandran S and Kristensen P 2013 *Nanophotonics* **2** 455

[6] Allen L, Padgett M J and Babiker M 1999 *Prog. Opt.* **39** 291

[7] Allen L, Beijersbergen M W, Spreeuw M W and Woerdman J P 1992 *Phys. Rev. A* **45** 8185

[8] Allen L 2002 *J. Opt. B* **4** S1

[9] Zhao C Y, Fan Y T, Meng Y C, Guo Q Z and Tan W H 2020 *Acta. Phys. Sin.* **69** 054207 (in Chinese)

[10] Mei X M and Huang J Z 2003 *Difference Geometry* (3rd edn.) (Beijing: Higher Education Press) pp. 51–53 (in Chinese)

[11] Schiff L I 1968 *Quantum Mechanics* (3rd edn.) (NewYork: McGraw-Hill Book Company) pp. 24–25

[12] Born M and Wolf E 2001 *Principles of Optics* (7th edn.) (Cambridge: World publishing Corporation) pp. 640–642

[13] Fang X Y, Ren H R and Gu M 2020 *Nat. Photon.* **14** 102

[14] Lao G M, Zhang Z H and Zhao D M 2016 *Opt. Express* **24** 18082

[15] Collins S A 1970 *J. Opt. Soc. Am.* **60** 1168

[16] Kogelnik H and Li T 1966 *Proc. IEEE* **154** 1312

[17] Wang Z X and Guo D R 2000 *Introduction of special functions* (Beijing: Beijing University) p. 415 (in Chinese)

[18] Gray D E 1957 *American Institute of Physics Hand book* (2nd edn.) (NewYork: McGraw-Hill Book Company) pp. 2–8